Cyclic Loading Experimental Investigation on Liquefaction and Post-Liquefaction Deformation of Stratified Saturated Sand

Zhanguo Xiu[1]; Shuhong Wang[2]; Yingchun Ji[3]; Feili Wang[4] and Fengyu Ren[5]

[1] School of Resources and Civil Engineering, Northeastern University, Shenyang city, China, **Email: xiuzhanguo109@126.com**

[2] School of Resources and Civil Engineering, Northeastern University, Shenyang city, China, **Email: wangshuhong@mail.neu.edu.cn**

[3] School of Science, Engineering & Environment, University of Salford, UK, **E-mail: Y.Ji@salford.ac.uk**

[4] Student, School of Resources and Civil Engineering, Northeastern University, Shenyang city, China, **Email: feili.wang@mail.utoronto.ca (Corresponding author)**

[5] School of Resources and Civil Engineering, Northeastern University, Shenyang city, China, **Email: renfengyu@mail.neu.edu.cn**

Abstract:

In fact, the soils are often distributed in a stratified structure. When an earthquake occurs, there are always risk of liquefaction for stratified soils which can cause serious consequences. The research aims to investigate the liquefaction and post-liquefaction deformation of saturated sand with stratified structure. The influences of liquefaction and post-liquefaction deformation were analyzed by varying the thickness, position and layers of powdery sands. The findings showed that the correlations between the times taken to reach liquefaction for cyclic loading and the thicknesses of the powdery sandy interlayer are non-linear. With the optimal thickness, the powdery sand interlayer can effectively prevent the transfer of power water pressure. And two-layer powdery interlayer in the sample was more favorable to resist pore water pressure than that with single layer. The strength

of post-liquefaction deformation and failure patterns are closely related to the distribution of powdery layer. The work provides new research evidence on the liquefaction and failure mechanism of saturated sands with stratified structure under cyclic loading which often happen during earthquakes.

Key words: Stratified structure; Saturated soils; Cyclic triaxial test; Pore water pressure; Liquefaction; Post-liquefaction deformation

Introduction

Previous studies have shown that liquefaction occurs when the pore water pressure inside saturated soils reaches the effective confining pressure which is one of the key factors influencing the nonlinear soils behavior (Sato et al. 1996; Aguirre and Irikura 1997; Kokusho et al. 2004; Peyman and Ali 2017). In short, the process of liquefaction with saturated soils happens when the effective stress between soil particles is gradually reduced to zero. The liquefaction of soils represents the complete loss of bearing capacity and the soils are in a flowing state. Most of the previous well-known liquefaction studies focused on homogeneous or well-mixed sand, but few on saturated sand with stratified structure (e.g., Zeghal and Shamy 2008; Constantine and Stamatopoulos 2010; Jia and Wang 2013; Karamitros et al. 2013; Arel et al. 2018; Huang et al. 2019). In natural geological environment, liquefiable soils with stratified structures are common (Li et al. 2019). Previous observations show that soils with stratified structures also experienced liquefaction during many earthquakes (Finn 1982; Amini and Qi 2000). It is therefore important to understand the liquefaction mechanism of stratified liquefiable soils and their failure forms after liquefaction has happened.

In more recent studies of soil liquefaction, many scholars have used uniform or uniformly mixed soils as their experimental objects or samples (e.g., Ecemis et al. 2015; Mandokhail et al. 2017; Javdanian 2019; Dammala et al. 2019). In order to determine the liquefaction properties of soils, a number of shaking table liquefaction tests (e.g., Carey et al. 2017; Jin et al. 2018; Chen et al.2019), cyclic triaxial tests (e.g., Pan and Yang 2018; Wang et al. 2018) and numerical simulations (e.g.,Ye and Wang 2016; Lei and Matthew 2018) were carried out with various forms of soil samples. Similar experimental studies, including Zhou et al. (2018), Bayat & Ghalandarzadeh (2019) and Huang & Zhao (2018), considered soil samples with different components, particle distribution and loading state, etc. It is worth noting that the above studies primarily focused on homogeneous or well-mixed sands, corresponding conclusions and laws may not necessarily be applicable to stratified structures. However, the liquefiable layered soils are also widely present (i.e., tailings dams, foundations of building and saturated sedimentary or alluvial strata), and the risk of liquefaction in such stratified structures also exists and can potentially cause catastrophic consequences. For experimental research studies on stratified soils, a few liquefaction tests have been performed on composite samples with layered structure (e.g., Elgamal et al. 1989; Kokusho and Kojima 2002; Chang et al. 2012; Jia and Wang 2013). The effect of drainage layer on the settlement of the composite samples have been investigated by Pradhan (1997). It was found that the presence of clay layer has little influence on the liquefaction strength of sand layer. A comprehensive experimental program was undertaken to compare the behavior of stratified and homogeneous silty sands during seismic liquefaction conditions (Amini and Qi 2000). The results indicated that the liquefaction resistances of layered and uniform soils were not significantly different. Yoshimine and Koike (2005) focused on the effects of stratified structure due to segregation of particle size and graded bedding in clean sand deposits on their liquefaction characteristics. The results demonstrated an underestimation of liquefaction resistance of deposits with laminar structure in situ when it was evaluated in the laboratory using homogeneously reconstituted samples. Ozener et al. (2008) presented the results of shaking table model tests and numerical modelling studies which were carried out to gain insight to liquefaction mechanisms in layered sand deposits. The results revealed that the presence of a less permeable silt interlayer within the sand deposit and existence of a loose sand layer underlying dense sand deposits can have significant effect on the liquefaction behavior. These existing studies discussed earlier indicated that the liquefaction and post-liquefaction deformation characteristics of the soils with layered structure are still in the exploration stage. And due to its unique structure and the high complex nature of liquefaction and post-liquefaction deformation under various uncertain conditions, currently there is lacking research evidence to form a general consensus within this research field.

When the liquefiable soils exist in the forms of layered structure, it is generally difficult to determine the liquefaction properties of multi-layered soils through the properties of one-layer soil. In general, the liquefaction properties of layered soils will be overestimated or underestimated by depending on the liquefaction evaluation criteria of a single layer of soil. Also, The post-liquefaction deformation directly affected by the failure forms and the extent of damage for the soils. The post-liquefaction deformation of the soils is also one of the important indicators for evaluating the liquefaction properties. Therefore, in this paper, the liquefaction mechanism, post-liquefaction strength and failure forms of saturated sandy samples with layered structure were studied. The research provides new evidence on the mechanism of seismic liquefaction and post-liquefaction deformation damage for layered soils.

Experimental methodology

Materials

The testing materials used in this research were two different sandy samples: fine and powdery sandy particles. The fine particles consists of pure sand with the particle size of 0.25~0.075mm. The powdery particle is composed of quartz flour with the particle size less than 0.075 mm. The particle size distributions of the tested materials were measured, and the measurements are presented in Fig. 1. Table 1 shows the key physical properties of the two types materials. According to the *Unified Soil Classification System* (USCS), the two types materials can be both considered as fine-grained soils. The shape of the two kinds of particles showed clear angular surface. For the fine particle, the angular surface is macroscopic. However, the angular surface of powdery material is observed by scanning electron microscope (SEM). The physical forms of the two materials are illustrated in Fig. 2.

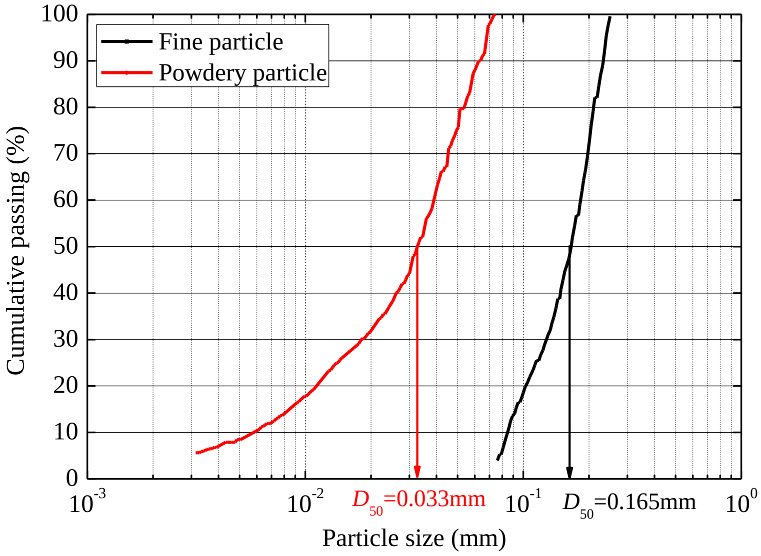

Fig.1. The curves of grain distribution

Table 1 Physical properties of the used materials.

Parameters	Unit	Fine-grained material	Powdery material
G_s (specific gravity)	-	2.665	2.705
D_{10} (particle size at 10% passing)	mm	0.085	0.0052
D_{30} (particle size at 30% passing)	mm	0.128	0.0179
D_{50} (particle size at 50% passing)	mm	0.165	0.0330
D_{60} (particle size at 60% passing)	mm	0.183	0.0385
D_{90} (particle size at 90% passing)	mm	0.231	0.0637
$C_u=D_{60}/D_{10}$ (coefficient of uniformity)	-	2.153	6.885
$C_c=(D_{30})^2/(D_{10}*D_{60})$ (coefficient of curvature)	-	1.053	1.600
$\Delta=(D_{90}-D_{10})/D_{50}$ (relative span factor)	-	0.885	1.773
Classification	-	Fine-grained soil	Fine-grained soil
$\rho_{s,}$ (density of the particles)	g/cm^3	2.621	2.699
e_{max} (the maximum void ratios)	-	1.058	1.705
e_{min} (the minimum void ratios)	-	0.656	0.867
Shape of soil particle	-	Angular surface	Angular surface

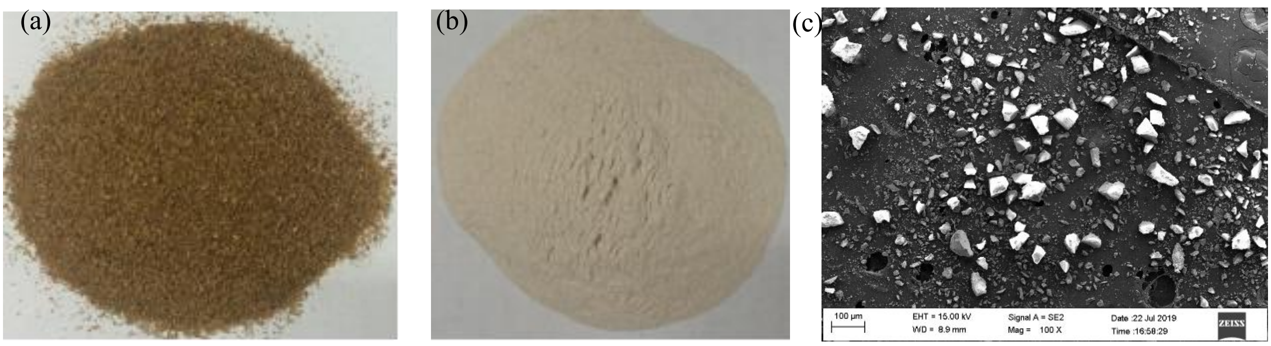

Fig. 2. The experimental materials. (a) Fine-grained material; (b) Powdery material; (c) The SEM image of

powdery material (magnified 100 times).

Equipment

The experimental equipment used in this research is the GCTS (*Geotechnical Consulting & Testing System*) STX-050 pneumatic triaxial testing system. Its highest hydraulic pressure is 1MPa, and 250kPa is its highest gas pressure. The axial displacement range is -25~25mm (this range is changeable). Conventional static and dynamic triaxial tests can be performed by the GCTS STX-050 system. And this testing system can achieve cyclic loading of sine, triangle and square waves under the stress or strain control with the maximum frequency 20 Hz. the system connection is shown in Fig. 3. It should be noted that the pore water pressure transducer is located at the bottom of the tested sample. The water connections in the lower part of the tested samples (shown in Fig. 3b) is connected to the pore water pressure transducer (shown in Fig. 3a). This means that the excess pore water pressure generated at the loading location needs to be transmitted throughout the whole sample and then reachs to the pore water pressure transducer.

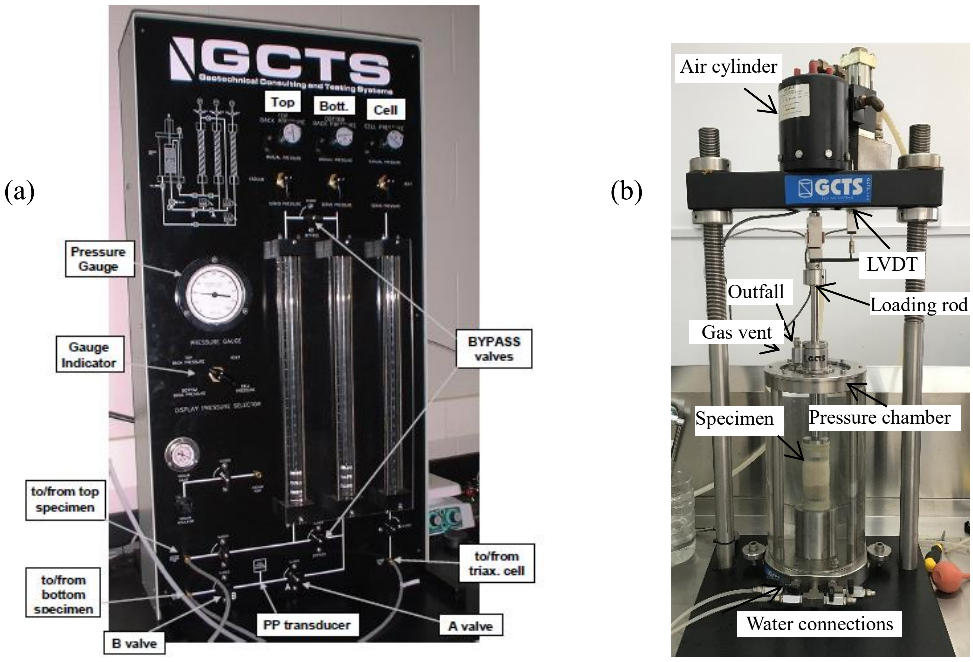

Fig. 3. The pneumatic triaxial connection system. (a) The diagram of control panel for the GCTS-STX-050 pneumatic triaxial testing system; (b) Actual diagram of the loading cell.

Testing program

The experimental sample is placed in a container and added the deaired water to the vacuum cylinder for pumping saturation (Skempton 1954). The sample preparation method is “soil sedimentation”, which greatly ensures the relative density of different sand layers are similar (Chen and Liu 2004; Jia and Wang 2013). Using this method, the mold with a stretched membrane was first filled with deaired water. Soil layers were then constructed by pluviating equal amounts of soil prepared before from the given height and waiting for at least 1 hour (about 2 hours for powdery sand) for them to settle. Stratified soil samples with given void ratios could be closely constructed using this method. At last, 5 kPa back pressure would be applied to the samples to make them stand straightly. The samples to be filled are divided into three categories. The first category, the thickness of the powdery sandy interlayer was controlled to be 0mm, 20mm, 40mm and 60mm separately, and this interlayer was positioned in the middle of the samples. The second category, powdery layer with a thickness of 40mm is located at the top, middle and bottom of the samples. The third category, 2×20mm two-layered distribution of powdery sand. Fig. 4 shows the typical triaxial testing samples. After constituting a sample, deaired water was circulated through the samples from the bottom to the top and suitable back pressure (50 kPa in this study) was applied in order to saturate the materials. That means that the remolding samples were saturated by hydraulic and back pressure combined method to ensure the Skempton’s B-value is equal to or greater than 0.95. It should be noted that the ratio of the increase in pore water pressure to the increase in confining pressure is Skempton’s B-value. The formula of Skempton’s B-value is shown in Eq.1. The tested samples shall be considered to be saturated if the Skempton’s B-value is equal to or greater than 0.95.

$$B - value = \frac{\Delta u}{\Delta \sigma_3} \tag{1}$$

Where, Δu is the increase in pore water pressure (kPa), and $\Delta \sigma_3$ is the increase in confining pressure (kPa). And the samples were isotropic consolidation (the first stage shown in Fig.5). The completed consolidation is determined when the drain valve was closed, and the pore water pressure no longer grows within 5 minutes period. The table 2 below shows the experimental models with the thickness, location and layers of the powdery sand in each

(a) (b)

model.

Fig. 4. The triaxial specimens preparation. (a) 60mm powdery interlayer; (b) 2×20mm powdery layers.

Table 2. Experimental models showing the thickness, location and layers of the powdery material in each model

Model no.	Powdery sandy layer										
	presence		locations			Thickness				Layers	
	No	Yes	Upper	Middle	Lower	20mm	40mm	60mm	100mm	One	Two
Model 1	√								√		
Model 2		√		√		√				√	
Model 3		√		√			√			√	
Model 4		√		√				√		√	
Model 5		√	√				√			√	
Model 6		√			√		√			√	
Model 7		√		√			√				√
Model 8		√	√		√		√				√

The diameter of testing samples is 50 mm, height is 100 mm (shown in Fig.4). The stratified sand samples are consisted of two different types of sands (fine sand and powdery sand). A summary of the stain-controlled undrained cyclic triaxial testing program and properties of tested samples are included in Table 3. The relative density of tested samples can be calculated by (Jia and Wang 2013):

$$D_{r,m} = \frac{e_{\max,m} - e}{e_{\max,m} - e_{\min,m}} \quad (2)$$

$$e_{\max,m} = \sum_{i=1}^{n}[R_{m,i}(e_{\max,i}+1)]-1, \quad e_{\min,m} = \sum_{i=1}^{n}[R_{m,i}(e_{\min,i}+1)]-1 \quad (3)$$

Where $R_{m,i}$, $e_{min,i}$, $e_{max,i}$ stands for the percentage of dry weight, maximum void ratio and minimum void ratio of i layer in the stratified soils, respectively.

Table 3 Properties of tested samples

Model no.	ρ_s/[g·cm^{-3}]	e	$D_{r,fine}$/[%]	$D_{r,powdery}$/[%]	$D_{r,m}$/[%]
Model 1	2.621	0.980	19.4		19.4
Model 2	2.637	1.042	18.9	82.1	30.3
Model 3	2.652	1.076	19.1	84.6	42.4
Model 4	2.668	0.985	18.2	85.2	69.9
Model 5	2.652	1.076	19.4	83.5	42.4
Model 6	2.652	1.076	18.2	85.1	42.4
Model 7	2.652	1.076	18.7	83.6	42.4
Model 8	2.652	1.076	19.2	82.4	42.4

The samples loading history curve is shown in Fig. 5. It can be clearly seen from Fig. 5, the loading history curve was divided into 3 stages. In general, liquefaction occurs mostly in shallow soil layers (within about 10 m). Therefore, the effective consolidation confining pressure selected at the first stage (isotropic consolidation) is 50 kpa. In this stage, we also assumed that the relative density of each sand layer is still at the same level after consolidation under an effective consolidation confining pressure of 50 kPa. After the isotropic consolidation, the second stage is the cyclic loading with the equal amplitude strain at 0.5% of whole sample height, and the frequency is 1 Hz. It should be noted that when the excess pore water pressure inside the test samples reaches the effective confining pressure ($\sigma_c^{'} = u$), then the sample was liquefied. The samples were liquefied after certain number of cyclic loading, then the third stage was carried out. The liquefied samples were subjected to an undrained static loading at a strain rate of 5% per minute to analysis the post-liquefaction deformation. The maximum loading displacement was set at 25%.

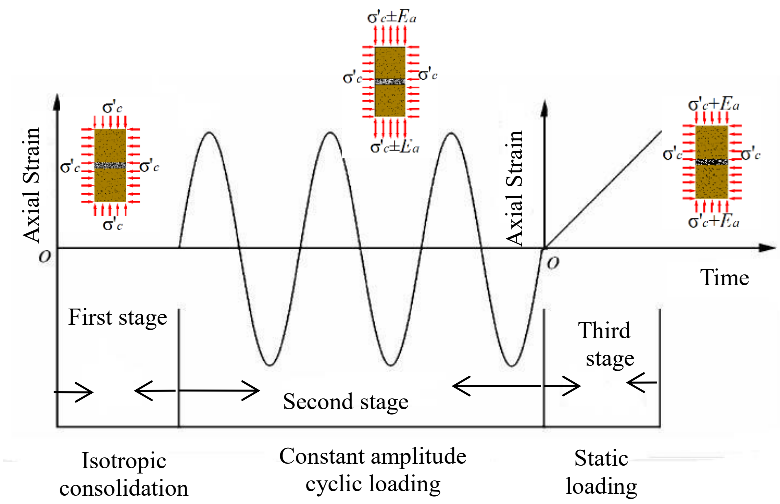

Fig. 5. Loading history curve

Results and Discussion

In this section, the test results and the subsequence analysis of liquefaction, post-liquefaction strength and failure forms will be presented against various experimental settings, such as varying thicknesses and locations of the powdery interlayer, as well as multiple interlayers. The post-liquefaction strength of the studied materials can be directly reflected by their deviator stress. And the development of post-liquefaction deviator stress is closely related to the pore water pressure. Therefore, the development of deviator stress and pore water pressure will be firstly examined to analyse the process of strength recovery. Then, the descriptions of the tested results and discussions of liquefaction, post-liquefaction strength and failure form with different samples will be followed.

Material post-liquefaction strength and pore water pressure under static loading

In this part, a pure fine particle sample (model 1) is taken as an example to investigate the development of its strength (deviator stress, Sd) and pore water pressure (PWP) under an undrained static loading at a strain rate of 5% per minute after liquefaction. In a triaxial test, the deviator stress is the difference between the major and minor principal stresses which is related to the axial load applied to the sample. Fig. 6 shows the deviator stress and pore water pressure changes of the sample during static loading after liquefaction (the final stage in Fig. 5). It should be noted that the change of the pore water pressure in Fig. 6 starting at 100 kPa. This is because that the sample has a back pressure of 50 kPa (As mentioned above) for reaching saturation before the cyclic loading.

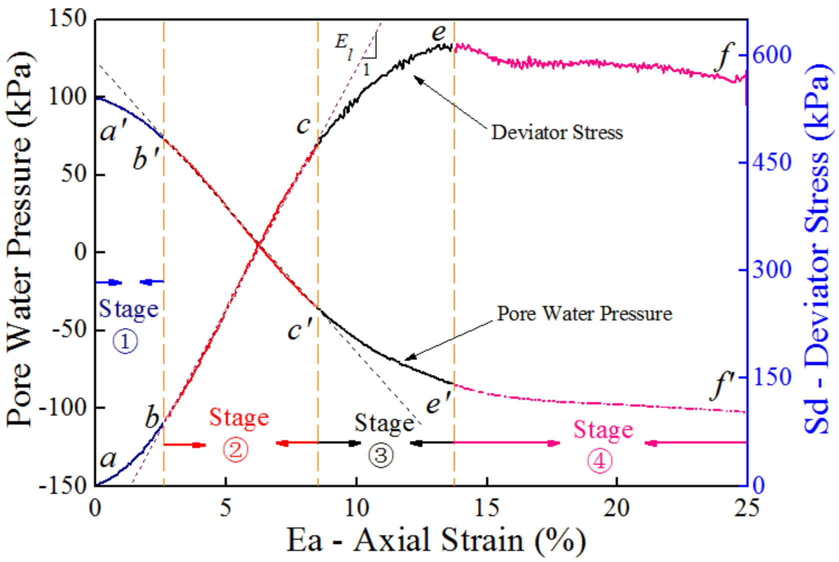

Fig.6. The deviator stress and pore water pressure curves of the sample during static loading after liquefaction

It is evident from Fig. 6 that the decrease of pore water pressure is associated with the increase of the deviatoric stress during the static loading test after liquefaction. And it can be clearly seen from Fig.6 that the two curves have a one-to-one relationship. From the changing tendency of the two curves, the development process of Sd and PWP can be roughly divided into four stages.

In the first stage (*a*-*b* section for Sd, *a′*-*b′* section for PWP), the initial pore water pressure (point *a′* shown in Fig. 6) is equal to confining pressure (σ_c), and the tangent modulus is also close to zero (point *a*). As the pore water pressure gradually dissipates, the deviator stress slowly increases. And the curve of deviator stress is the concave type. The *a*-*b* is the material strength recovery stage. The second stage (*b*-*c* and *b′*-*c′* section for Sd and PWP), the pore water pressure almost linearly dissipates and in the meanwhile, the deviator stress increases. The slope of the deviatoric stress curve is the elastic modulus (E_l shown in Fig.6) of the sample after liquefaction. And the *b*-*c* segment is regarded as the elastic phase. The third stage (*c*-*e* and *c′*-*e′* section for Sd and PWP), with the increase of axial displacement, the decrease of pore water pressure and the growth rate of deviatoric stress were slowing down. Then the unrecoverable plastic deformation was formed. The *c*-*e* segment is therefore regarded as the plastic phase. During the fourth stage (*e*-*f* and *e′*-*f′* section for Sd and PWP), after reaching the peak strength (point *e*), the sample enters the failure stage. Then, with the increase of axial displacement, the pore water pressure and deviatoric stress are no longer changing significantly.

Effect of powdery interlayer with different thickness

The influences of powdery interlayer with the different thickness on liquefaction and post-liquefaction deformation were examined using Models 1 to 4 in Table 1 (see Table 1, with interlayer thickness at 0 mm, 20 mm, 40 mm & 60 mm). Fig. 7 depicts the changes of the pore water pressure *u* (kPa) with the number of loading cycles *N* under the constant amplitude strain cyclic loading.

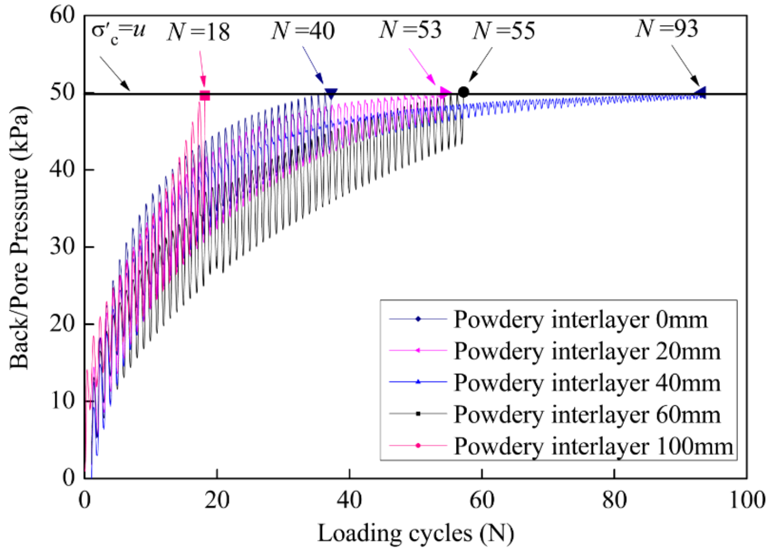

Fig.7. Relationship between pore water pressure and number of loading cycles with different thicknesses of powdery interlayer.

The black line ($\sigma'_c=u$) is a the liquefied marker in Fig. 7. It can be seen from Fig. 7 that the pore water pressure shows different growth trends under the constant amplitude strain cyclic loading when the thicknesses of interlayer are different. Broadly speaking, the powdery interlayer reduces the growth rate of pore water pressure, more loading cycles are needed to reach the effective confining pressure (σ'_c), and in the meantime liquefaction is resulted. When varying the thickness of the interlayer from 0 mm, 20 mm, 40 mm, and 60 mm (ref. Models 1~4), the numbers of loading cycles required for liquefaction are 40, 53, 93, and 55 times, respectively.

With Models 2 and 4 (20 mm and 60 mm interlayers), the loading cycles required to reach liquefaction are similar, while model 3 with 40 mm interlayer needed more loading cycles to reach liquefaction. It is clear that the number of loading cycles needed to reach liquefaction are not linearly correlated with the thicknesses of the interlayer. This phenomenon was also confirmed in Jia and Wang's study (Jia and Wang 2013). It is also evident that an optimal thickness of the interlayer exists which can maximize the loading cycles/times required to reach liquefaction. When the thickness of the powder interlayer is less than the optimal thickness, more loading cycles are needed with the increase of the interlayer thickness. On the contrary, when the interlayer thickness is larger than the optimal thickness, numbers of loading cycles needed to reach liquefaction are decreased with the increase of the interlayer thickness. From the microscopic perspective, due to the presence of the powdery interlayer, the permeability of the whole sample will be changed. The permeability of the powdery layer is lower than that of the fine layer, which requires more loading cycles to break the powdery structure (Huang and Zhao 2018). In addition, when the pore water pressure encounters the powdery layer with smaller permeability, the powdery layer slows down the transport of pore water pressure. With the increases of the powdery layer, the powdery interlayer plays a more significant role in the samples. The smaller size materials are more liable to liquefy than the bigger ones under the same loading conditions (Lee et al. 2015). When the thickness of the powdery interlayer is larger than the optimal thickness, it can accelerate the rate of liquefaction, and cause a decrease in the required loading cycles for liquefaction. In order to explain that the liquefaction can be accelerated when the thickness of the powdery interlayer is larger than the optimal thickness, the liquefaction test of the 100 mm powdery sand is added in this study. The test result was shown in the Fig. 7. The test result shows that the sample can be liquefied only by 18 loading cycles. This means that under the same conditions, powdery sand is easier to liquefy than fine sand. And the powdery interlayer can both hinder and accelerate liquefaction. This depends on the thickness of the powdery interlayer.

After the consolidation and liquefaction processes were completed, the samples were subjected to the static loading with the strain rate of 5% per minute under undrained condition. With the static loading, the pore water pressure of the samples is gradually decreased, the deviatoric stress or strength are gradually recovered (shown in Fig.6). Fig. 8 shows the deviator stress and normalized pore water pressure curves of the samples with different thickness of powdery interlayer during static loading after liquefaction.

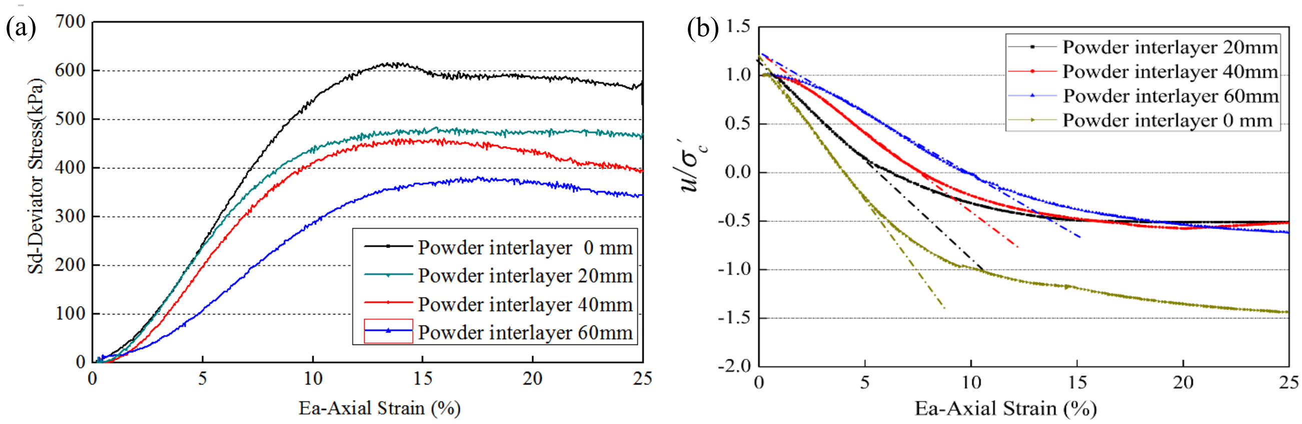

Fig. 8. The deviator stress and normalized pore water pressure curves of the samples with different thickness of powdery interlayer during static loading after liquefaction. (a) Relationship of axial strain and deviator stress; (b) Relationship of axial strain and normalized pore water pressure..

As shown in Fig. 8(a), when the thickness of the powdery interlayer is increased, the peak value of the deviatoric stress will be decreased. This indicates that the presence of the powdery interlayer can significantly affect the large deformation strength of the sample after liquefaction. The difference in compression and dilatancy properties of the two materials in the tested samples have a large effects on the overall failure mode of the samples. For example, when the thickness of powdery interlayer is 60mm (model 4), the peak value of deviator stress is significantly reduced, which is related to the failure form of the samples (ref: Fig. 9). And it also can be seen from Fig. 8(b), With the continuous thickening of the powdery interlayer (from 0 mm to 60 mm), the slope of the normalized pore water pressure curve gradually decreases. This indicates that the decrease rate of the pore water pressure is weakened due to the presence of the powdery interlayer. This phenomenon is caused by the presence of a lower permeability powdery interlayer which changes the permeability of the whole samples. For the 4 cases examined (Model 1 to 4) there are differences in the failure forms under axial static loading after liquefaction. Fig. 9 shows the failure forms of samples with the different thickness of powdery interlayer under axial static loading after liquefaction.

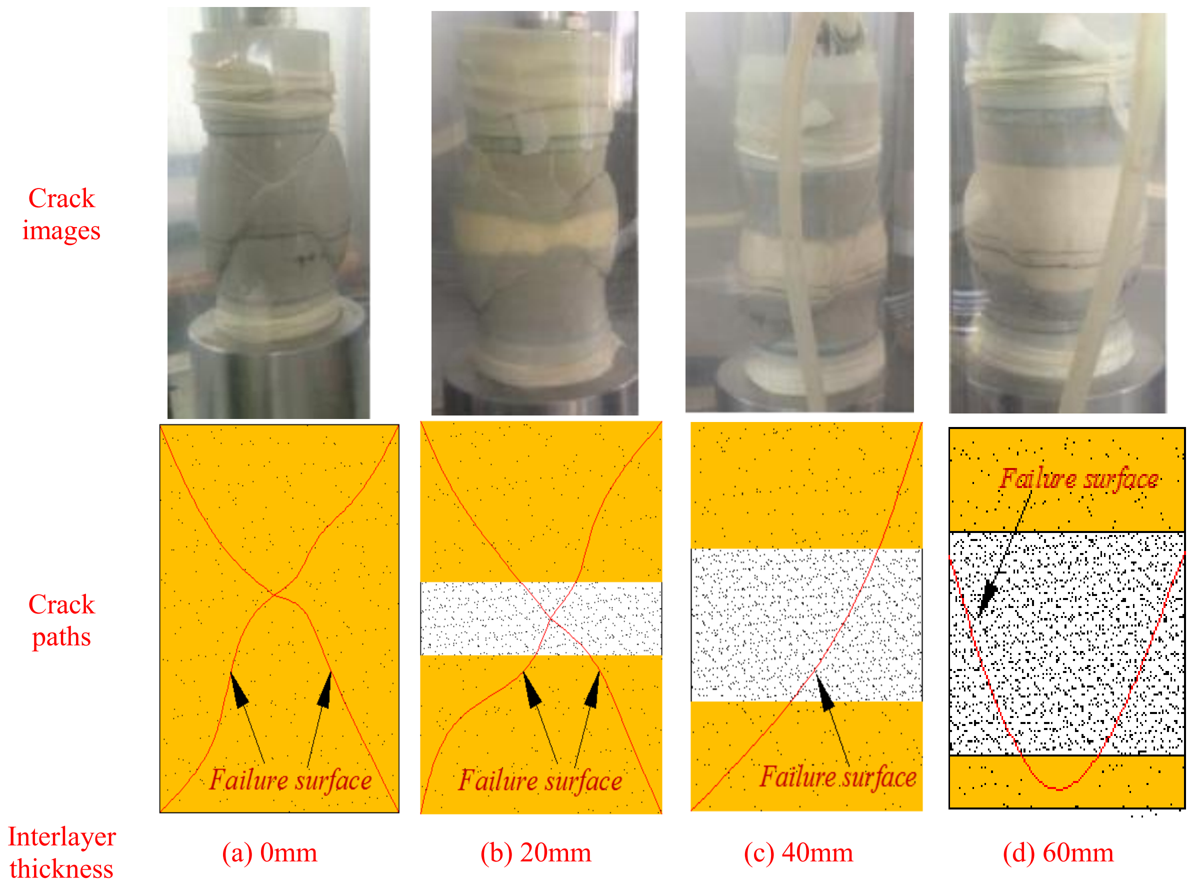

Fig. 9. The failure forms with different thickness of powdery interlayer under axial static loading

The fracture form of saturated uniform fine-grained sample (model 1) showed double main cracks with an "X" shape as shown in Fig. 9(a) under axial static loading after liquefaction. When the powdery interlayer is at 20mm (model 2), the dilatancy zone of the sample is not affected by the interface between the two different materials, and the entire interlayer was completely dilated. The failure form is similar to the uniform fine-grained sample (model 1) with an “X” shape. At the intersection of the cracks, the deformation of the powdery layer is obvious, as shown in Fig. 9(b). When the powdery interlayer is at 40mm (model 3), the fracture form becomes single diagonal crack, and the crack starts from the fine-grain layer as shown in Fig. 9(c). It indicates that the powdery and fine particles are filled with each other during the liquefaction process between their interfaces. And the interfaces between the two different materials are relatively stable. When the interlayer is at 60mm (model 4), the dilatation zone is the powdery layer, and the initial crack located at the powdery layer rather than at the interface between the two different materials. Two diagonal cracks with an "V" shape are generated in the powdery area, as shown in Fig. 9(d). Fig. 9 clearly shows that the presence of the powdery interlayer has an important influence on the failure forms under the axial static loading after liquefaction.

Effect on the powdery sand with different locations

According to the above research, when the thickness of the powdery interlayer is 40mm, the sample has the best resistance to liquefaction. Therefore, the influences of the powdery interlayer locations on liquefaction and post-liquefaction deformation were examined using the 40 mm thickness powdery interlayer Models 3 (middle), 5 (top) & 6 (bottom) in Table 1. The relationships of the pore water pressure *u* and the number of cyclic loading cycles *N* for these samples under constant amplitude strain cyclic loading is shown in Fig. 10.

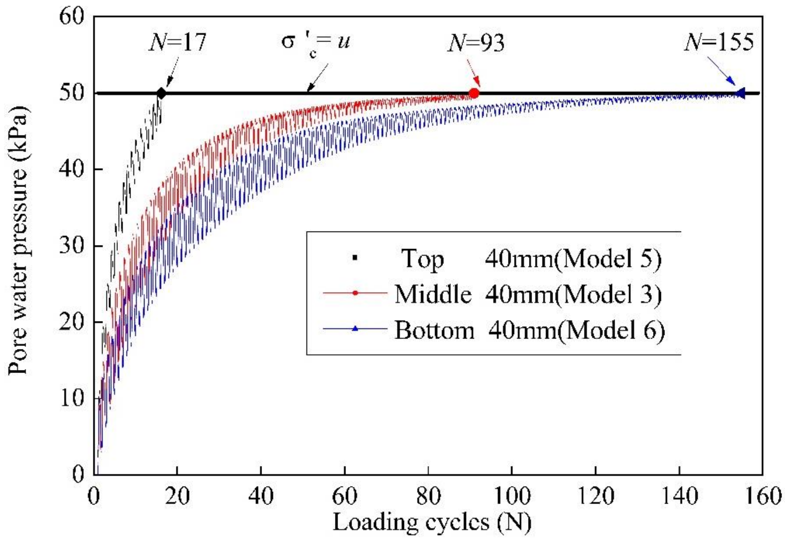

Fig. 10. Relationship of loading cycles and pore water pressure with different locations of powder layer

The different locations of powdery interlayer have obvious influences on the growth of pore water pressure. When the powdery layer is located on the top (model 5), the sample is liquefied by reaching to effective confining pressure (σ'_c) after only 17 loading cycles. The particle size of powdery material is much smaller than fine particle, which leads to a rapid increase of the pore water pressure under the same cyclic loading in the powdery layer. For model 5, the pore water pressure is rapidly generated in the powdery layer on the top of the sample. The fine-grain layer beneath the powdery layer has a relatively large permeability, the transmission of pore water pressure is relatively easy. When the powdery layer located at the middle (model 3), the sample was liquefied after 93 loading cycles. Compared with Model 5, the pore water pressure is effectively blocked by the low-permeability powdery interlayer. When the powdery layer is located at the bottom (model 6), the pore water pressure is generated in the fine-grain layer. The particle size of the fine-grain material is bigger than powdery material, it is not easy to liquefy under the same conditions. And due to the effective blockage of the bottom powdery layer, more loading cycles (N=155) are needed to reach liquefaction under the same loading conditions. The testing results show that the obstruction of fine-grained layer on the pore water pressure generated by the powdery layer can be neglected, while the obstruction of the powdery layer on the pore water pressure generated by the fine-grained layer is obvious.

An undrained axial static loading tests were performed on the liquefied samples with different locations of powdery layer. The different failure forms under static loading after liquefaction are shown in fig. 11. When the 40 mm powdery layer is located at the top (model 5 in table 1), the dilatation zone is the fine-grain layer, and the interface of two different materials is located at the top edge of the dilatancy zone, as shown in Fig. 11(a). With the development of dilatancy deformation, the interface is firstly destroyed, and the crack develops downward from the interface. When the powdery layer is located at the middle (model 3), a main diagonal crack is present as shown in Fig. 11(b). When the powdery layer is located at the bottom (model 6), the dilatation zone is fine layer, and the interface is located at the bottom edge of the dilatation zone. And the interface is firstly destroyed, showing a "shedding" type of failure form, as shown in Fig. 12(c). According to the testing results, when the powder layer is located at the top and bottom of the samples, the interface has strong influences on the failure forms.

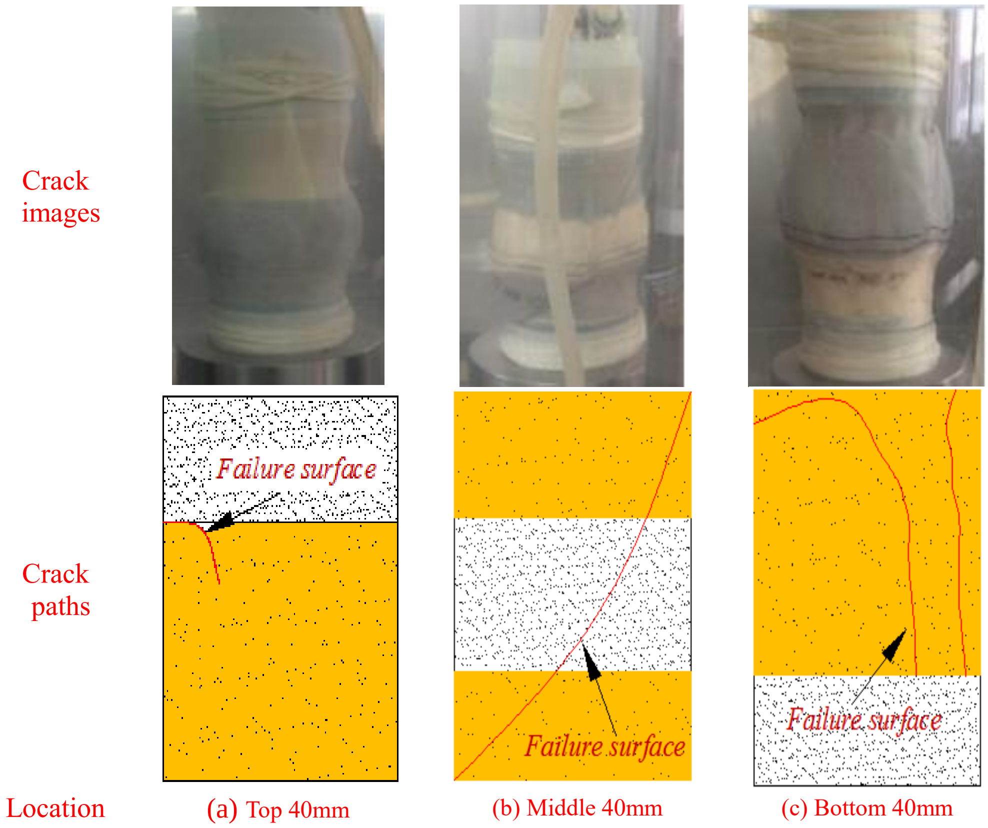

Fig. 11. The static loading failure forms under different locations of powdery layer

Based on the consideration of different positions of powdery layer in testing samples, the deviator stress and normalized pore water pressure curves of the samples with different locations of powdery sand during static loading after liquefaction were shown in Fig. 12.

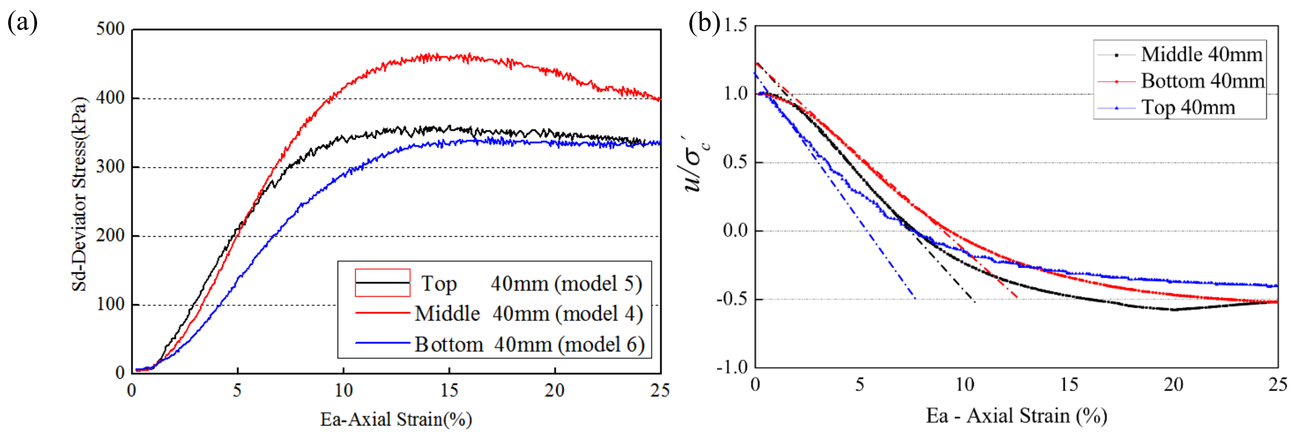

Fig. 12. The deviator stress and normalized pore water pressure curves of the samples with different locations of powdery sand during static loading after liquefaction. (a) Relationship of axial strain and deviator stress; (b) Relationship of axial strain and normalized pore water pressure.

From, the Fig. 12(a), it can be clearly seen that the post-liquefaction deformation strength (Sd) of the samples with different positions of powdery layer is quite different. When the 40mm powdery layer is located at the middle (model 3 in table 1), the strength is significantly higher than that at the top and bottom. This is reflected by the failure forms of the samples. When the powdery layer is located at the top (model 5) and the bottom (model 6), the failure occurs at the interface between the two different materials (shown in fig.11a, 11c). When the powdery layer is at the middle, the failure occurs across the powdery layer diagonally. This implicates that the failure forms of the samples directly influence the deformation strength after liquefaction. It also can be seen from Fig. 12(b), although the thickness of the powdery sand is same in the samples, there is still a significant difference in the decrease rate of the pore water pressure due to the different positions of powdery sand. This result shows that the position of the powdery sand in the samples can significantly affect the decrease of the pore water pressure. When the powdery layer is located at the bottom of the sample, it can effectively hinder the decrease of pore water pressure, and its decrease rate is the slowest. This is because the pore water pressure is effectively hindered by the lower permeability powdery sand during the decrease process. However, when the powdery sand is at the top of the sample, the larger permeability of the fine sand at the bottom has no obvious effect on the pore water pressure, and the pore water pressure decrease at the fastest rate.

Effect on the powdery sand with two layers

The effect of two-layer distribution of powdery particles on the liquefaction and the post-liquefaction deformation was also examined. Two testing samples (model 7 in table 1: five layers from bottom to top, two layers of 20mm powdery sands separated by 20mm fine sands in the middle (refer Fig.15a); Model 8: from bottom to top are powdery layer 20mm, fine-grain layer 60mm and powdery layer 20mm, respectively, see Fig. 15b). The relationship between the cyclic loading times and pore water pressure of the samples with two-layer powdery layers, as shown in fig.13.

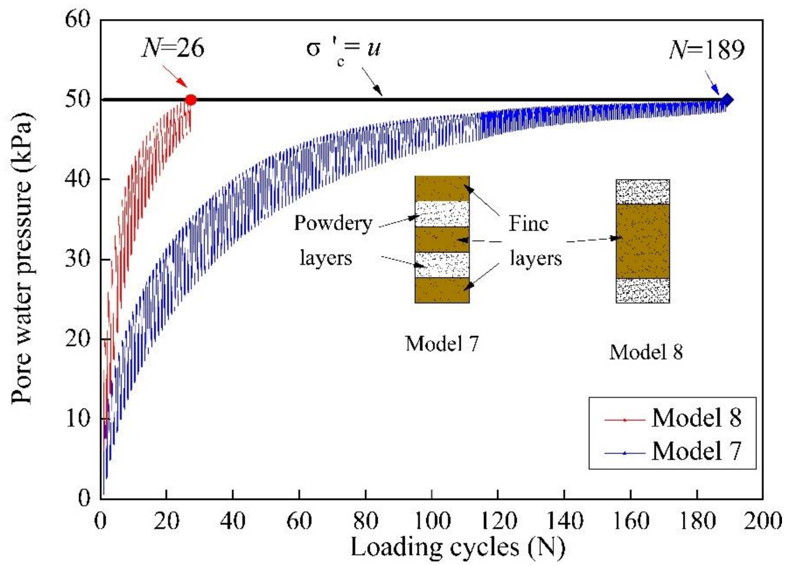

Fig. 13. Relationship of loading cycles and pore water pressure with two-layer powdery layers

Model 7 requires 189 loading cycles to reach the effective confining pressure (σ'_c), then the sample was liquefied. However, only 26 loading cycles were needed for model 8 to reach the liquefied state. The required loading cycles for the two samples are significantly different. The pore water pressure of model 8 was generated in the top fine-grained layer, while for model 7 this was produced in the powdery layer. The two-layer distribution of the powdery layer (20mm each, model 7, 189 loading cycles before liquefaction) is more effective in blocking pore water pressure than single layer (40mm, model 3, 93 loading cycles) distribution. By comparing model 4 (60mm powdery layer as an interlayer, 55 loading cycles) and model 8 (60mm fine-grained layer as an interlayer, 26 loading cycles), the powdery interlayer tends to have relatively larger resistance to liquefaction than that of the fine-grained interlayer.

The liquefied samples were then subjected to axial static loading. The deviator stress and normalized pore water pressure curves of the samples with two-layer powdery sand during static loading after liquefaction were shown in Fig. 14.

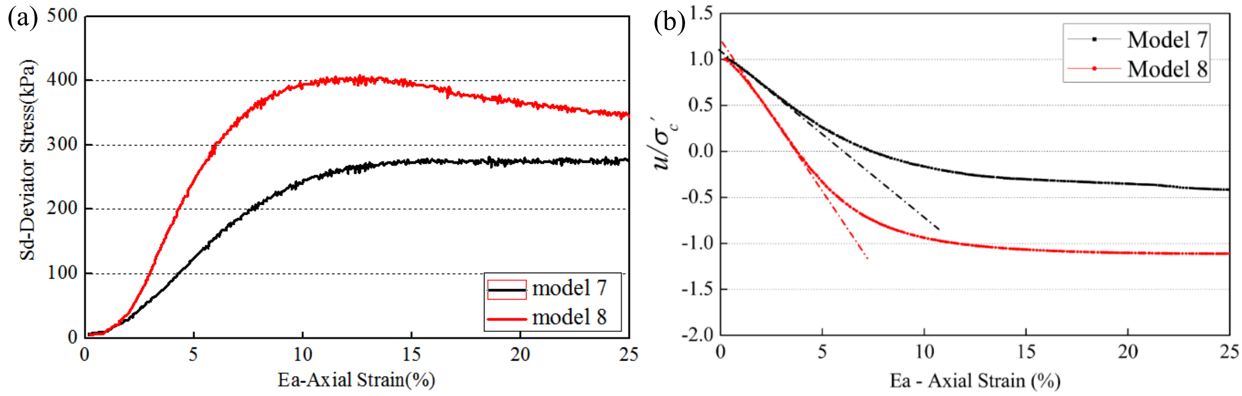

Fig. 14. The deviator stress and normalized pore water pressure curves of the samples with two-layer powdery sand during static loading after liquefaction. (a) Relationship of axial strain and deviator stress; (b) Relationship of axial strain and normalized pore water pressure.

The strength (reflected by the deviator stress of materials) to resist post-liquefaction deformation for model 7 is significantly higher than that of model 8, as shown in Fig. 14(a). This is also thought to be due to the differences in failure forms. Fig. 15 shows the failure forms of two specimens under static axial loading.

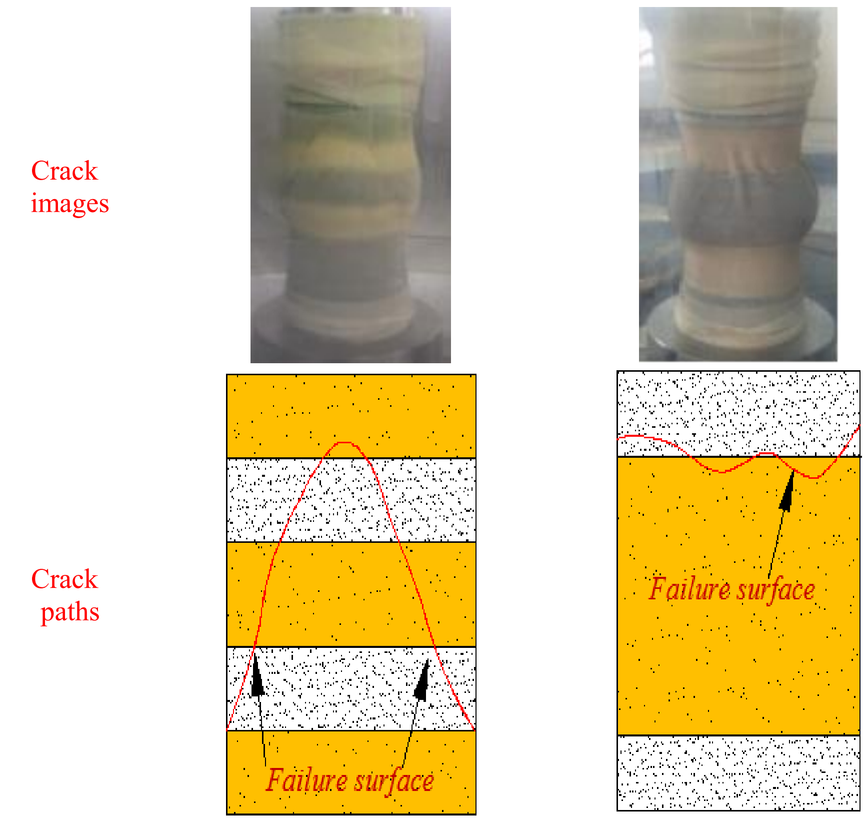

Model No. (a) model 7 (b) model 8

Fig. 15. The static loading failure forms of model 7 and 8 after liquefaction

The failure crack of model 7 appears at the interface of the bottom edge of dilatancy zone. The second powdery interlayer was firstly destroyed, and the two main cracks present an inverted "V" shape. The powdery and fine layers had obvious fault in the failure zone. Due to the destruction of the interface, the dilatancy zone has not been fully developed, resulting the lower strength of model 7. The dilatancy zone of model 8 was within the fine-grain layer, and two interfaces between the two materials are the top and bottom boundaries of dilatancy zone. As the axial strain increase, the failure produced at the top boundary. The whole sample exhibits a "plug-in" failure form. The sample is fully compressed, and its compressive strength is fully utilized. Similarly, as can be seen from Fig. 14(b), the pore water pressure decrease rate of Model 8 is significantly faster than that of Model 7. This shows that the two-layer powdery sand at the middle of the sample has a significant hindrance to the decrease of pore water pressure. However, when the middle layer is fine sand, the hindrance to the pore water pressure is not obvious.

Conclusions

In this study, the triaxial experiments were carried out by using GCTS-STX-050 dynamic triaxial testing system to study the liquefaction and post-liquefaction deformation of saturated sand with stratified structure. Different thicknesses, locations and layers of powdery and fine sands were considered in the testing samples. The key findings are as follows:

(1) When considering the different thickness of the powdery interlayer in the testing samples, the results show that the presence of the powdery interlayer can effectively hinder the transmission of excess pore water pressure. The cyclic loading required for liquefaction is nonlinear with the thickness of powdery interlayer. There is an optimal thickness that can potentially maximize the number of cyclic loading required for liquefaction. The failure forms of post-liquefaction deformation are closely related to the thickness of the powdery interlayer. Thicker powdery interlayer leads to a higher strength under static loading after liquefaction.

(2) When the powdery layer is located at different positions of the stratified samples, the results show that the

powdery layer can effectively block the transmission of pore water pressure generated by the fine-grained layer. However, the fine-grained layer does not effectively hinder the transmission of pore water pressure generated by the powdery layer. The failure forms of post-liquefaction deformation were greatly restricted by the interface between the two different materials.

(3) The distribution of two-layer powdery interlayer sand in the sample was more favorable to resist pore water pressure than that with single layer. And the powdery layer as an interlayer has larger resistance to liquefaction than that fine-grained layer as an interlayer.

The research findings clearly demonstrated that the existence of smaller particle layer may speed up or slow down the process of liquefaction, the relative thickness and distribution of the smaller particle layers also have significant influences on the deformations of materials. From the testing results in this study, it is expected to reduce the possibility of soil liquefaction by changing the structure for the liquefiable soil (e.g. add a low permeability interlayer, etc.) in the engineering practice . Also, these findings show firsthand research evidence on material strength of various types of layered soils, they provide practical implications on judging the geological stability of regions with similar layered soils structures.

Acknowledgments

This work was conducted with supports from the National Natural Science Foundation of China (Grant Nos. U1602232 and 51474050), the Fundamental Research Funds for the Central Universities (Grant No. N17010829), Doctoral Scientific Research Foundation of Liaoning Province (Grant No. 20170540304 and 20170520341). Liaoning Science and Technology Project (2019JH2/10100035). Also, many thanks to associate prof. Chun Li in the guidance presented in the work.

References

Aguirre J, Irikura K (1997) Non-linearity, liquefaction, and velocity variation of soft soil layers in Port Island, Kobe, during the Hyogoken-Nanbu earthquake. Bull Seism Soc Am 87:1244-1258

Amini F, Qi GZ (2000) Liquefaction testing of stratified silty sands. J Geotech. Geoenviron Eng 126(3):208-217

Arel E, Onalp A, Olgun GC (2018) The effect of clay mineral content on the dynamic response of reconstituted fine grained soil. B Earthq Eng 16(10):4515-4532

Bayat M, Ghalandarzadeh A (2019) Influence of depositional method on dynamic properties of granular soil. Int J Civ Eng 17(6):907-920

Carey JM, Mcsaveney MJ, Petley DN (2017) Dynamic liquefaction of shear zones in intact loess during simulated earthquake loading. Landslides 14(3):789-804

Chang M, Kuo CP, Hsu RE, Shau SH, Lin TM (2012) Liquefaction potential and post-liquefaction settlement evaluations of the Chuoshui River Alluvial Fan in Taiwan. Bull Eng Geol Environ 71(2):325-336

Chen GX, Liu XZ (2004) Study on dynamic pore water pressure in silty clay interbedded with fine sand of Nanjing. J Geotech Eng 01:79-82 (in Chinese)

Chen HE, Jiang YL, Niu CC, Leng GJ, Tian GL (2019) Dynamic characteristics of saturated loess under different confining pressures: a microscopic analysis. Bull Eng Geol Environ 78:931–944

Constantine A, Stamatopoulos (2010) An experimental study of the liquefaction strength of silty sands in terms of the state parameter. Soil Dyn Earthq Eng 30:662-678

Dammala PK, Kumar SS, Krishna AM, Bhattacharya S (2019) Dynamic soil properties and liquefaction potential of northeast Indian soil for non-linear effective stress analysis. B Earthq Eng 17(6):2899-2933

Ecemis N, Demirci HE, Karaman M (2015) Influence of consolidation properties on the cyclic re-liquefaction potential of sands. B Earthq Eng 13(6):1655-1673

Elgamal A, Dobry WR, Adalıer K (1989) Small scale shaking table tests of saturated layered sand-silt deposits. Proc 2nd US-Japan Workshop on Soil Liquefaction, Buffalo 233-245

Finn WDL (1982) Fundamental aspects of response of tailing dams to earthquakes. Dyn Stability of Tailing Dams, ASCE Nat Convention, ASCE, New York, 46-72

Huang Y, Yang Y, Wang L (2019) Evolution of anti-liquefaction performance of foundation soils after dam construction. Bull Eng Geol Environ 78(1): 641-651

Huang Y, Zhao L (2018) The effects of small particles on soil seismic liquefaction resistance: current findings and future challenges. Nat. Hazards 92:567-579

Javdanian, Hamed (2019) Evaluation of soil liquefaction potential using energy approach: experimental and statistical investigation. Bull Eng Geol Environ 78(3):1697-1708

Jia MC, Wang BY (2013) Liquefaction testing of stratified sands interlayered with silt. Appl Mech Mater 256-259:116-119

Jin JX, Song CG, Liang B, Chen YJ, Su ML (2018) Dynamic characteristics of tailings reservoir under seismic load. Environ Earth Sci 77:654

Karamitros DK, Bouckovalas GD Chaloulos YK, Andrianopoulos KI (2013) Numerical analysis of liquefaction-induced bearing capacity degradation of shallow foundations on a two-layered soil profile. Soil Dyn Earthq Eng 44(1):90-101

Kokusho T, Hara T, Hiraoka R (2004) Undrained shear strength of granular soils with different partical gradations. J Geotech Geoenviron Eng 130(6):621-129

Kokusho T, Kojima T (2002) Mechanism for postliqefaction water film generation in layered sand. J Geotech Geoenviron Eng 128(2):129-137

Lee JH, Shibuya S, Lohani TN, Wakamoto T, Kataoka S (2015) Effect of grain-size distribution on cyclic strength of granular soils. Proc Computer Methods and Recent Advances in Geomechanics. Kyoto, Japan, 699-703

Lei Z, Matthew ET (2018) Boundary effects in discrete element method modeling of undrained cyclic triaxial and simple shear element tests. Granular Matter 20(4):60

Li C, Xiu ZH, Ji YC, Wang FL, Chan AHC (2019) Analyzing the Deformation of Multilayered Saturated Sandy Soils under Large Building Foundation. KSCE J Civ Eng 23(9):3764-3776

Mandokhail SUJ, Park D, Yoo JK (2017) Development of normalized liquefaction resistance curve for clean sands. B Earthq Eng 15(3):907-929

Ozener PT, Ozaydin K, Berilgen M (2008) Numerical and physical modeling of liquefaction mechanisms in layered sands. Proc Geotechnical Earthquake Engineering and Soil Dynamics IV Congress, Sacramento, CA, United States: American Society of Civil Engineers.

Pan K, Yang ZX (2018) Effects of initial static shear on cyclic resistance and pore pressure generation of saturated sand. Acta Geotech 13(2):473–487

Peyman A, Ali P (2017) Liquefaction-induced settlement of shallow foundations on two-layered subsoil strata. Soil Dyn Earthq Eng 94:35-46

Pradhan TBS (1997) Liquefaction behavior of sandy soil sandwiched by clay layers. Proc 7th International Offshore and Polar Engineering Honolulu, HI, 676-682.

Sato K, Kokusho T, Matsumoto M, Yamada, E (1996) Nonlinear seismic response and soil property during strong motion. Soils Found 36:41-52

Skempton AW. (1954) The pore pressure coefficients A and B. Geotechnique 4(4):143-147.

Wang JX, Deng YS, Shao YL, Liu XT, Bo F, Wu LB, Zhou J, YIN Y, Xu N, Peng HH (2018) Liquefaction behavior of dredged silty-fine sands under cyclic loading for land reclamation: laboratory experiment and numerical simulation Environ Earth Sci 77: 471

Ye JH, Wang G (2016) Numerical simulation of the seismic liquefaction mechanism in an offshore loosely deposited seabed. Bull Eng Geol Environ 75(3):1183-1197

Yoshimine M, Koike R (2005) Liquefaction of clean sand with stratified structure due to segregation of particle size. Soils Found 45(4):89-98

Zeghal M, Shamy U E (2008) Liquefaction of saturated loose and cemented granular soils. Powder Technol 184(2):254-265

Zhou YG, Liu K, Ling DS, Shen T, Chen YM (2018) Threshold seismic energy and liquefaction distance limit during the 2008 Wenchuan earthquake. Bull Eng Geol Environ 16(11):5151–5170